TECHNICAL ARTICLE

Structural Design and Mechanical Properties Analysis of Fused Triply Periodic Minimal Surface Porous Scaffold

Shoujin Zeng ⬤, Weihui He, Jing Wang, Mingsan Xu, and Tieping Wei

In the field of bone tissue engineering, additive-manufactured metal scaffolds based on triply periodic minimal surfaces (TPMS) are expected to become a substitute for bone injury repair. The bone scaffolds based on the triply periodic minimal surfaces are similar in shape to natural bone tissue and also have many advantages in terms of strength and permeability, which have become one of the research hotspots in the field of additive manufacturing of metal scaffolds in recent years. In this study, the research of the mechanical properties and porosity of the fused TPMS porous bone scaffold provides us with a predictive tool to assist the design of the bone scaffold. First, porous bone scaffold models are established by fusing two different TPMS units, and the samples are manufactured by selective laser melting technology and subjected to quasi-static compression test. The response surface method is used to analyze the effects of TPMS unit constants K_1, K_2, and fused boundary r on the mechanical properties and porosity of the porous scaffold, and the optimal structural parameters of multiple response targets are obtained by optimization. The results show that the most ideal design parameters are $K_1 = 10.000$, $K_2 = 2.656$, $r = 5.564$, and the yield strength of the fused porous structure is 400.962 Mpa, the elastic modulus is 10.532 GPa, and the porosity is 64.027%, the error between the optimized result and the predicted result is very small. In summary, the porous bone scaffold with high yield strength and low elastic modulus is manufactured by fusion of TPMS, which provides an effective method for the application of bone substitutes.

1. Introduction

Bone transplantation is widely used to repair bone defects in clinic. At present, there is a great demand for bone transplantation at home and abroad. At least 2.2 million bone transplants are performed worldwide every year. Among them, the treatment of segmental bone defects, especially in weight-bearing areas, is a complex process in orthopedic surgery (Ref 1). In order to meet the needs of the bone graft market, synthetic metal bone scaffolds are used as bone graft substitutes. Because titanium alloy has good mechanical properties and corrosion resistance, titanium alloy is commonly used clinically as a metal material for bone defect repair (Ref 2, 3), but the elastic modulus of titanium alloy is 110 GPa, which is much larger than that of human bone (10–30 GPa). Long-term implantation of solid titanium alloy scaffolds will produce stress shielding effect, and the bone tissue will shrink due to the reduction of mechanical tension, which will cause fractures at the implantation site (Ref 4, 5). Lee et al. (Ref 6, 7) prepared biomimetic titanium scaffolds with different pore characteristics, which effectively alleviated the stress shielding effect, and

the scaffolds had the property of releasing multiple biomolecules to effectively maintain osteocyte differentiation. Therefore, in order to reduce the elastic modulus of the scaffold, the scaffold can be designed as a porous structure.

Predecessors have done a lot of research on the structural design of porous scaffolds, Sahu et al. (Ref 8, 9) used CAD software to design porous scaffold models with different pores and studied the effect of pores on the mechanical properties of the structure. Lee et al. (Ref 10) fabricated titanium alloy scaffolds by the dynamic freeze-casting method and post-treated with HF/HNO3, and the pore size was conveniently controlled by changing the post-treatment time. Wang et al. (Ref 11) studied the effects of different pore structures on cell proliferation and vascularization by designing regular and irregular porous structures. EI-Sayed et al. (Ref 12, 13) studied the effect of design parameters on the mechanical properties of porous structures and optimized the unit size to fabricate porous structures that match the characteristics of human bone. Compared with these design methods, TPMS is a simple and effective mathematical method to define pore structure. It can design different structural units and pore sizes according to requirements and has high connectivity and smooth surface. It has become a favorable tool for porous scaffolds of bone tissue engineering (Ref 14, 15).

People are more and more interested in research on TPMS. Yang et al. (Ref 16) designed homogeneous porous structure of G unit with different volume fractions and explored the influence of volume fraction of G unit on the mechanical properties of porous structure. Bobbert et al. (Ref 17) designed and manufactured different titanium alloy porous structures based on four different types of triply periodic minimal surfaces. The results showed that the porous structure of TPMS

Shoujin Zeng, Weihui He, Jing Wang, Mingsan Xu, and **Tieping Wei,** School of Mechanical and Automotive Engineering, Fujian University of Technology, Fuzhou 350118, China. Contact e-mail: zengshoujin@fjut.edu.cn.

Al	V	O	N	C	H	Fe	Ti
6.13	3.95	0.065	0.012	0.006	0.005	0.12	Bal

can not only reduce the stress shielding effect, but also provide adequate mechanical support for bone tissue regeneration and osseointegration. However, in order to obtain porous structures that is more similar to natural bone tissue, further research is still needed. From a macropoint of view, it is unreasonable to establish porous scaffolds with uniform porosity. Yang et al. (Ref 18) designed and manufactured G unit structures with different gradient directions. The results showed that the gradient distribution makes the structure have new deformation modes and mechanical properties. Surmeneva et al. (Ref 19) designed five different types of layered porous titanium alloy scaffolds to simulate the structure of human trabecular bones. The experiments showed that the scaffold with layered gradient pores have good ductility. Xiong et al. (Ref 20) fabricated four layered functionally graded scaffolds with different structures. The experimental results showed that the elastic modulus of the samples was similar to that of cortical bone. The high porosity area in the inner layer of natural bone tissue guarantees the regeneration and growth of cells and tissues, while the low porosity area in the outer layer improves the bearing capacity of bone. The porous structure with hierarchical distribution can better meet the requirements of mechanical properties and biocompatibility. Therefore, it is also particularly important to design a layered porous scaffold similar to human bone.

In addition, with the development of additive manufacturing technology (Ref 21), the manufacturing of complex porous structure becomes simple. At present, additive manufacturing technology has been applied to the manufacture of bone tissue engineering scaffolds. Among them, selective laser melting technology has great advantages (Ref 22, 23). The characteristics of layer-by-layer accumulation forming can realize the forming of almost any complex structure and can accurately control the spatial structure of scaffolds to meet the needs of bone tissue engineering scaffolds.

Considering the above requirements for the bearing capacity of bone tissue, if the TPMS unit type is used to design the porous structure, the mechanical properties cannot be well met. By fusing two different TPMS unit types, the outer layer uses a unit to increase the bearing capacity, so that the porous scaffold has appropriate strength to bear the physiological load, and the inner layer uses another unit to increase the inner surface area to provide more growth area for cells. Both the inner and outer layers have porous structure, allowing cell growth and transportation of nutrients and wastes, so as to design a porous scaffold with good mechanical properties and appropriate porosity. In addition, the influence of unit structure and porosity on the performance of porous scaffolds is also complex. How to adjust the structural design parameters of porous scaffolds to achieve the balance of performance is also one of the current research directions of orthopedics medicine. Therefore, based on the triply periodic minimal surfaces (TPMS), porous scaffold model with layered structure is designed through the fusion of Diamond unit and Gyroid unit. The samples are prepared by selective laser melting technology and compres-
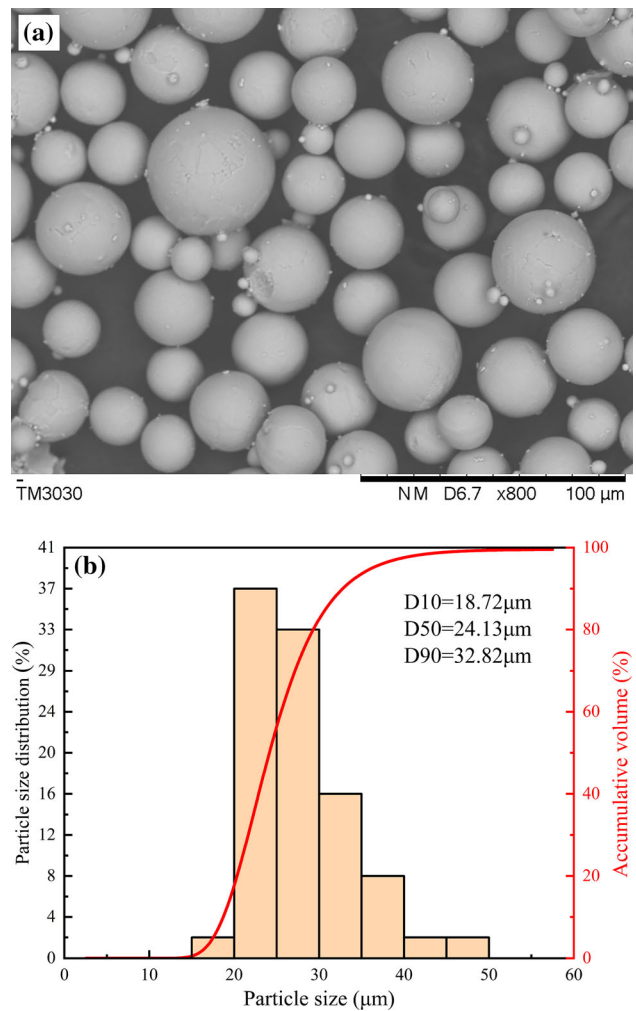
Fig. 1 (a) SEM micrograph and (b) particle size distribution of Ti6Al4V alloy powder

sion experiments are carried out. Then the response surface method is used to analyze the influence of constants K_1, K_2 and the fused boundary r on the mechanical properties of the porous scaffold. The results provide a basis for the design of porous scaffolds in orthopedics.

2. Experimental Method and Structure Design of Porous Scaffold

2.1 Experimental Materials and Equipment

Table 1 shows the chemical composition of the titanium alloy powder. Figure 1 shows the SEM micrograph and particle size distribution of the powder. The SEM micrograph shows a nearly spherical shape of the powder (Fig. 1a), and the particle size distribution ranging from 18.72 (D10) to 32.82 μm (D90) (Fig. 1b). The experimental platform is the SLM-125HL forming equipment developed by SLM Solution in Germany. Laser forming process is performed under the protection of argon gas, and the forming principle is shown in Fig. 2. Powder is evenly spread on the substrate, and powder layer is melted by a high energy laser. The laser scans one layer and the forming
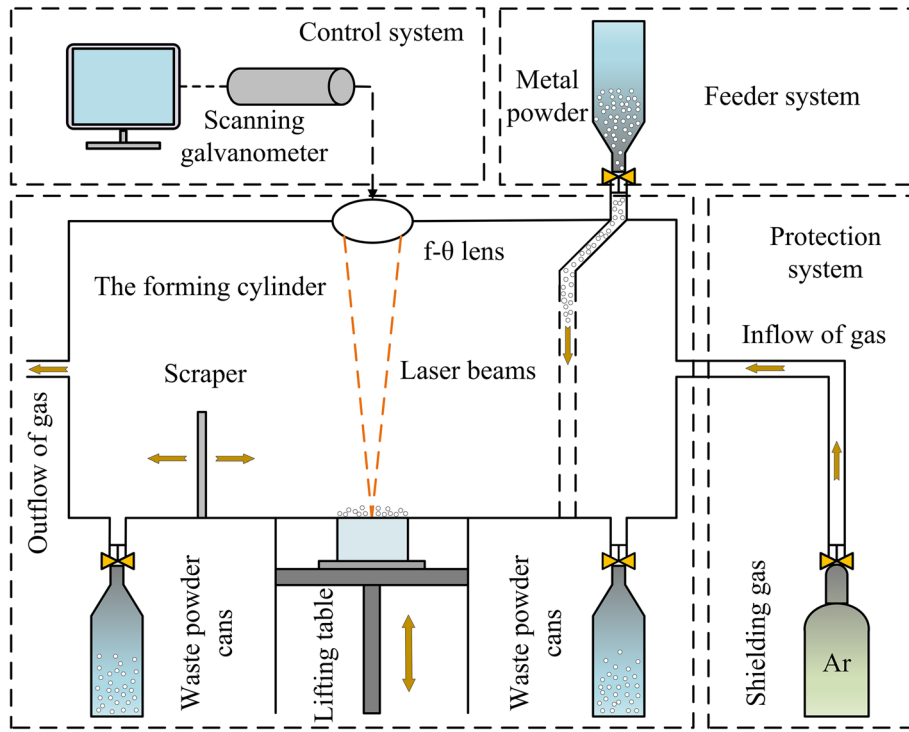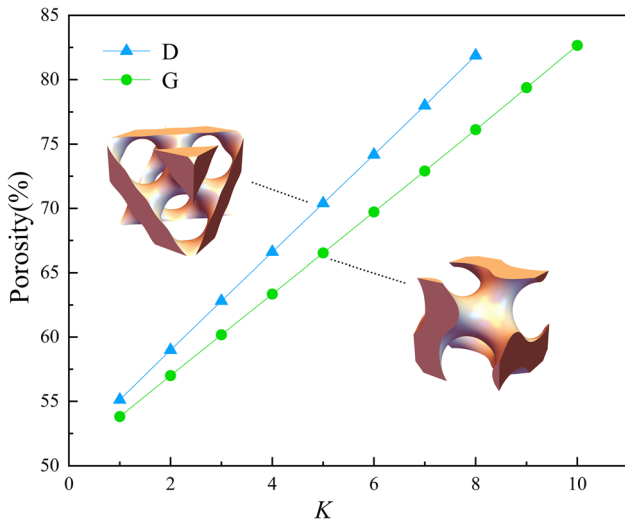
Fig. 2 Forming principle diagram of SLM

Fig. 3 The relationship between the porosity P and the constant K of the G and D units

chamber drops one layer. This process is repeated until the sample is completed. The process parameters used in this article are laser power 275 W, scanning speed 1100 mm/min, scanning layer thickness 30 μm, and scanning pitch 0.12 mm.

2.2 Homogeneous Porous Scaffold Design

TPMS is a kind of minimal surface with periodicity in three independent directions in three-dimensional space (Ref 24, 25). There are many kinds of common TPMS surfaces. In order to

better simulate the structure of bone tissue, the following two types of TPMS surfaces are selected in this paper, namely G (gyroid) surface and D (diamond) surface. The unit shape formed by the G curved surface is similar to cancellous bone, and the unit structure formed by the D curved surface has a good bearing capacity. Its basic equations are as follows:

$$
\begin{aligned}
\varphi_G(x,y,z) = 10\left[\cos\left(\frac{2\pi}{\omega}x\right)\sin\left(\frac{2\pi}{\omega}y\right) + \cos\left(\frac{2\pi}{\omega}y\right)\sin\left(\frac{2\pi}{\omega}z\right)\right. \\
\left. + \cos\left(\frac{2\pi}{\omega}z\right)\sin\left(\frac{2\pi}{\omega}x\right)\right] - 0.5\left[\cos\left(\frac{4\pi}{\omega}x\right)\cos\left(\frac{4\pi}{\omega}y\right)\right. \\
\left. + \cos\left(\frac{4\pi}{\omega}y\right)\cos\left(\frac{4\pi}{\omega}z\right) + \cos\left(\frac{4\pi}{\omega}z\right)\cos\left(\frac{4\pi}{\omega}x\right)\right] - K
\end{aligned}
$$

(Eq 1)

$$
\begin{aligned}
\varphi_D(x,y,z) = 0.6\left[\cos\left(\frac{8\pi}{\omega}x\right) + \cos\left(\frac{8\pi}{\omega}y\right) + \cos\left(\frac{8\pi}{\omega}z\right)\right] \\
- 10\left[\sin\left(\frac{2\pi}{\omega}x\right)\sin\left(\frac{2\pi}{\omega}y\right)\sin\left(\frac{2\pi}{\omega}z\right)\right. \\
+ \sin\left(\frac{2\pi}{\omega}x\right)\cos\left(\frac{2\pi}{\omega}y\right)\cos\left(\frac{2\pi}{\omega}z\right) \\
+ \cos\left(\frac{2\pi}{\omega}x\right)\sin\left(\frac{2\pi}{\omega}y\right)\cos\left(\frac{2\pi}{\omega}z\right) \\
\left. + \cos\left(\frac{2\pi}{\omega}x\right)\cos\left(\frac{2\pi}{\omega}y\right)\sin\left(\frac{2\pi}{\omega}z\right)\right] - K
\end{aligned}
$$

(Eq 2)

where (x, y, z) are the three directions of the rectangular coordinate system, ω is the period of the curved surface, and K is a constant. The shape of the curved surface can be influenced by controlling the constant K. When the equation is greater than
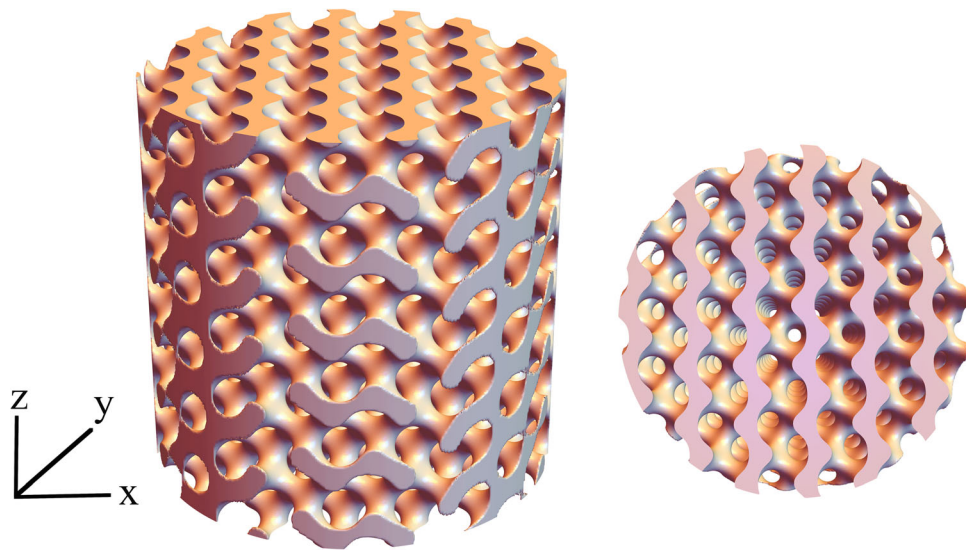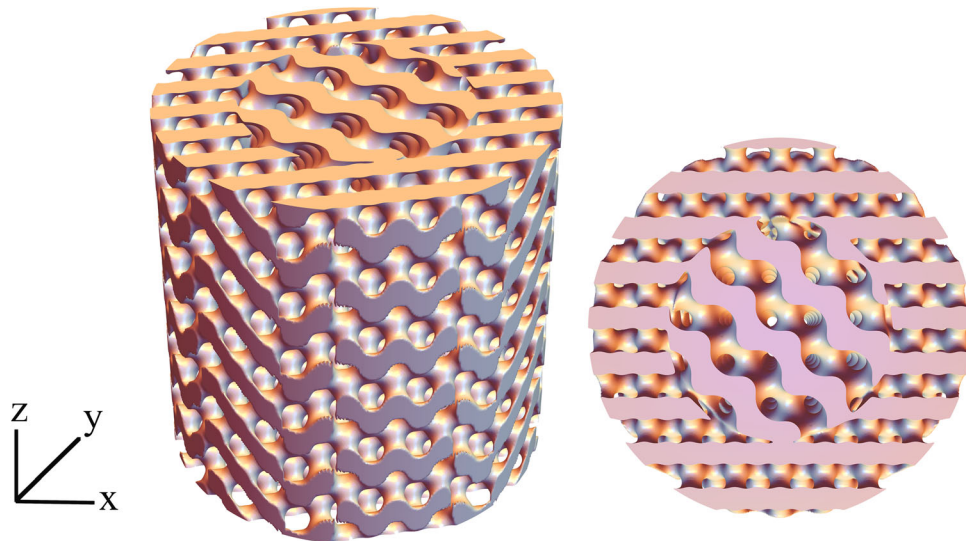
Fig. 4 Model of unit G
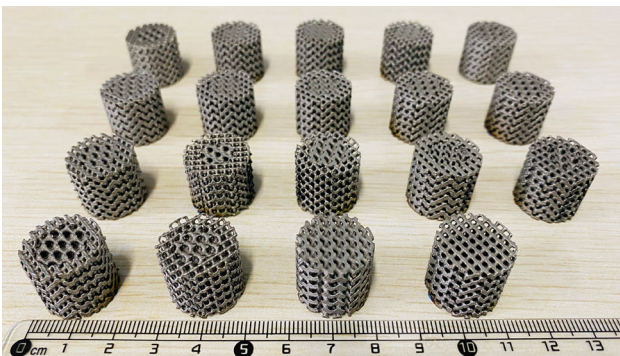

Fig. 5 Fused model of unit G and D

Fig. 6 Ti6Al4V porous structure samples manufactured by SLM

or less than 0, the TPMS unit structure is formed. The pores of TPMS structure can be characterized by porosity, which refers to the percentage of the internal pore volume of the material in its total volume. The formula for calculating the porosity of the TPMS unit in this paper is:

$$P = \frac{V_0 - V}{V} \times 100\% \qquad \text{(Eq 3)}$$

where P is the porosity of TPMS unit structure (%); V_0 is the total volume of the cell (mm^3); V is the volume enclosed by the TPMS curved surface bounding box.

The value ranges of G shaped surface function (2) and D shaped surface function (3) are $[-10,13]$, $[-7,11]$, respectively. In order to ensure the growth of bone tissue, the porosity should be controlled between 50 and 90% (Ref 26). Therefore, the constant K of the G-shaped surface functional formula is set to $[1, 10]$, and the constant K of the D-shaped surface functional formula is set to $[1, 8]$. Figure 3 shows the relationship between the porosity P and the constant K of the two TPMS units.

The TPMS unit obtained by TPMS function, and then the modeling of porous structure of G unit is completed by
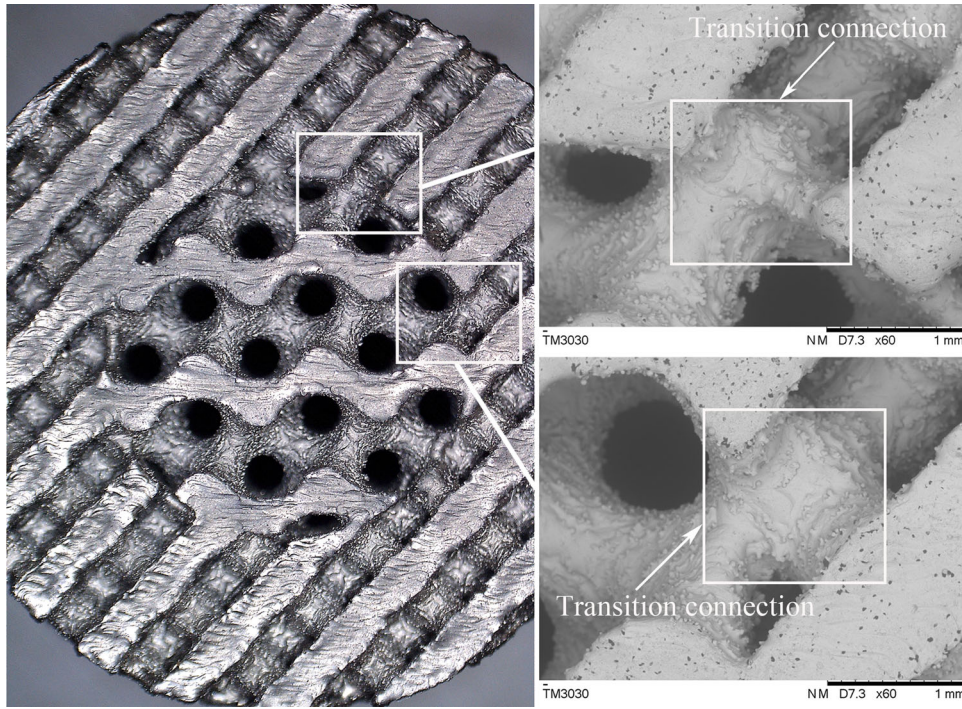
Fig. 7 SEM image of the fused area between the G and D unit

Table 2 The factors and level of response surface

Factor	Level		
	− 1	0	1
K_1	1	5. 5	10
K_2	1	4.5	8
r	4.5	5.25	6

Wolfram Mathematic 12.0 software. Its model is shown in Fig. 4.

2.3 Fused Porous Scaffold Design

TPMS unit in the previous section is used to construct fused porous scaffold model. The fused part has a transition area with porous morphology, and the transition of the fused part may be transformed by mutation or smoothing. According to the paper of Yang et al (Ref 27), it is possible to describe the fused porous structure based on TPMS equation by using a continuous function. Here, the fused structure between two TPMS unit types is considered, there is

$$\varphi_{\text{hyb}}(x, y, z) = \varphi_1(x, y, z)\beta + \varphi_2(x, y, z)(1 - \beta) \qquad \text{(Eq 4)}$$

where φ_1 and φ_2 are the basic equations of TPMS, β is the weighted distribution function, and the range of values is [0, 1]. Yang et al. (Ref 27) gave a sigmoid function to describe the monotonic change of β from 0 to 1, and the function expression is:

$$\beta(x, y, z) = \frac{1}{1 + e^{-tG(x,y,z)}} \qquad \text{(Eq 5)}$$

In the formula, t is the transition coefficient, which can control the transition between the two pore structures in the

fused zone. Considering the continuity of the overall structure and reducing the discontinuity or sudden connection change of the fusion area, this paper selects $t = 2.5$ with reference to the research of Yang (Ref 27). At this time, the smooth connection of two TPMS units can be achieved, and $G(x, y, z)$ is the boundary that describes the fused area. The equation for constructing the fused porous structure using the G and D unit models is:

$$\varphi_{\text{hyb}}(x, y, z) = \left(10 \left[\cos\left(\frac{2\pi}{\omega}x\right) \sin\left(\frac{2\pi}{\omega}y\right) \right.\right.$$
$$+ \cos\left(\frac{2\pi}{\omega}y\right) \sin\left(\frac{2\pi}{\omega}z\right) + \cos\left(\frac{2\pi}{\omega}z\right) \sin\left(\frac{2\pi}{\omega}x\right) \right]$$
$$- 0.5 \left[\cos\left(\frac{4\pi}{\omega}x\right) \cos\left(\frac{4\pi}{\omega}y\right) + \cos\left(\frac{4\pi}{\omega}y\right) \cos\left(\frac{4\pi}{\omega}z\right) \right.$$
$$\left. + \cos\left(\frac{4\pi}{\omega}z\right) \cos\left(\frac{4\pi}{\omega}x\right) \right] - K_1 \right) \frac{1}{1 + e^{-tG(x,y,z)}}$$
$$+ \left(0.6 \left[\cos\left(\frac{8\pi}{\omega}x\right) + \cos\left(\frac{8\pi}{\omega}y\right) + \cos\left(\frac{8\pi}{\omega}z\right) \right] \right.$$
$$- 10 \left[\sin\left(\frac{2\pi}{\omega}x\right) \sin\left(\frac{2\pi}{\omega}y\right) \sin\left(\frac{2\pi}{\omega}z\right) \right.$$
$$+ \sin\left(\frac{2\pi}{\omega}x\right) \cos\left(\frac{2\pi}{\omega}y\right) \cos\left(\frac{2\pi}{\omega}z\right)$$
$$+ \cos\left(\frac{2\pi}{\omega}x\right) \sin\left(\frac{2\pi}{\omega}y\right) \cos\left(\frac{2\pi}{\omega}z\right)$$
$$+ \cos\left(\frac{2\pi}{\omega}x\right) \cos\left(\frac{2\pi}{\omega}y\right) \sin\left(\frac{2\pi}{\omega}z\right) - K_2 \right)$$
$$\left(1 - \frac{1}{1 + e^{-tG(x,y,z)}} \right)$$

$$\text{(Eq 6)}$$

Table 3 Experimental results

Number	K_1	K_2	r	Yield strength/MPa	Apparent elastic modulus/GPa	Porosity/%
1	1	1	5.25	475.72	12.2	49.82
2	1	4.5	4.5	364.51	10.39	59.12
3	1	4.5	6	420.67	11.75	57.65
4	1	8	5.25	342.53	8.73	66.88
5	5.5	1	4.5	470.14	12.13	54.53
6	5.5	1	6	432.19	11.91	55.95
7	5.5	4.5	5.25	366.67	10.32	63.20
8	5.5	4.5	5.25	361.50	10.05	63.32
9	5.5	4.5	5.25	380.22	10.29	63.28
10	5.5	4.5	5.25	360.18	9.96	63.80
11	5.5	4.5	5.25	377.86	10.04	62.19
12	5.5	8	4.5	236.71	8.12	72.30
13	5.5	8	6	275.79	8.55	71.04
14	10	1	5.25	447.13	11.94	58.95
15	10	4.5	4.5	378.18	10.01	66.25
16	10	4.5	6	330.84	9.24	69.89
17	10	8	5.25	219.16	7.34	76.63

Table 4 Variance analysis of yield strength

Project	Sum of squares	Degree of freedom	Mean square	F value	$P > F$ value	
Source	84,395.58	9	9377.29	56.02	< 0.0001	Significant
K_1	6504.84	1	6504.84	38.86	0.0004	
K_2	70,498.25	1	70,498.25	421.14	< 0.0001	
r	12.38	1	12.38	0.074	0.7935	
$K_1 \times K_2$	2245.81	1	2245.81	13.42	0.0080	
$K_1 \times r$	2678.06	1	2678.06	16.00	0.0052	
$K_2 \times r$	1483.41	1	1483.41	8.86	0.0206	
K_1^2	495.29	1	495.29	2.96	0.1291	
K_2^2	340.81	1	340.81	2.04	0.1967	
r^2	182.40	1	182.40	1.09	0.3313	
Residual	1171.79	7	167.40			
Lack of fit	828.34	3	276.11	3.22	0.1444	Not significant
R-squared	0.9863		Pred R-squared	0.8388		
Adj R-squared	0.9687		Adeq Precision	24.667		

Table 5 Variance analysis of elastic modulus

Project	Sum of squares	Degree of freedom	Mean square	F value	$P > F$ value	
Source	34.20	9	3.80	70.64	< 0.0001	significant
K_1	2.58	1	2.58	47.89	0.0002	
K_2	29.80	1	29.80	553.92	< 0.0001	
r	0.080	1	0.080	1.49	0.2622	
$K_1 \times K_2$	0.32	1	0.32	5.93	0.0450	
$K_1 \times r$	1.13	1	1.13	21.08	0.0025	
$K_2 \times r$	0.11	1	0.11	1.96	0.2039	
K_1^2	8.621×10^{-3}	1	8.621×10^{-3}	0.16	0.7009	
K_2^2	0.066	1	0.066	1.22	0.3062	
r^2	0.12	1	0.12	2.27	0.1757	
Residual	0.38	7	0.054			
Lack of fit	0.27	3	0.091	3.44	0.1316	not significant
R-squared	0.9891		Pred R-squared	0.8696		
Adj R-squared	0.9751		Adeq Precision	28.079		

Table 6 Variance analysis of porosity

Project	Sum of squares	Degree of freedom	Mean square	F value	$P > F$ value	
Source	763.53	9	84.84	250.69	< 0.0001	Significant
K_1	182.88	1	182.88	540.41	< 0.0001	
K_2	571.22	1	571.22	1687.93	< 0.0001	
r	0.68	1	0.68	2.01	0.1997	
$K_1 \times K_2$	0.096	1	0.096	0.28	0.6106	
$K_1 \times r$	6.53	1	6.53	19.29	0.0032	
$K_2 \times r$	1.80	1	1.80	5.31	0.0547	
K_1^2	0.10	1	0.10	0.31	0.5952	
K_2^2	0.020	1	0.020	0.061	0.8127	
r^2	0.22	1	0.22	0.64	0.4491	
Residual	2.37	7	0.34			
Lack of fit	0.98	3	0.33	0.94	0.5018	Not significant
R-squared	0.9969		Pred R-squared	0.9768		
Adj R-squared	0.9929		Adeq Precision	59.310		

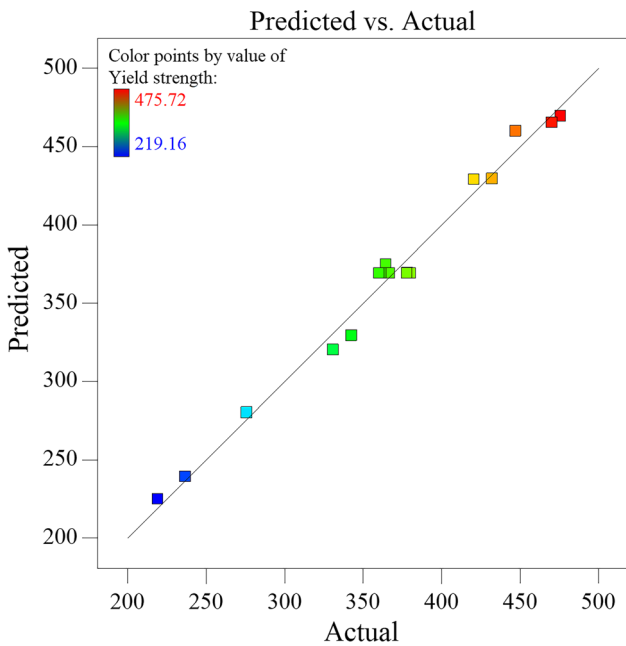Fig. 8 The predicted value and actual value of the yield strength

Fig. 9 The predicted value and actual value of the elastic modulus

Its fused model is shown in Fig. 5, where: $K_1 = K_2 = 1$, $G(x, y, z) = 5.25^2 - x^2 + y^2$.

2.4 Measurement Method and Mechanical Performance Test

The sample produced by SLM forming is shown in Fig. 6. After the printing was completed, the sample was cut by the electric discharge machine, then used an ultrasonic cleaning machine to remove the residual titanium alloy powder in the samples, and finally put them into a dryer for drying. In this paper, the weight method is used to measure the average porosity of the sample:

$$\overline{P} = \frac{V_1 - V_2}{V_1} \times 100\% = \left(1 - \frac{\frac{m}{\rho}}{\pi r^2 H}\right) \times 100\% \quad \text{(Eq 7)}$$

where V_1 is the volume of a solid cylinder with the same outer dimensions of the sample, and V_2 is the volume of the sample,
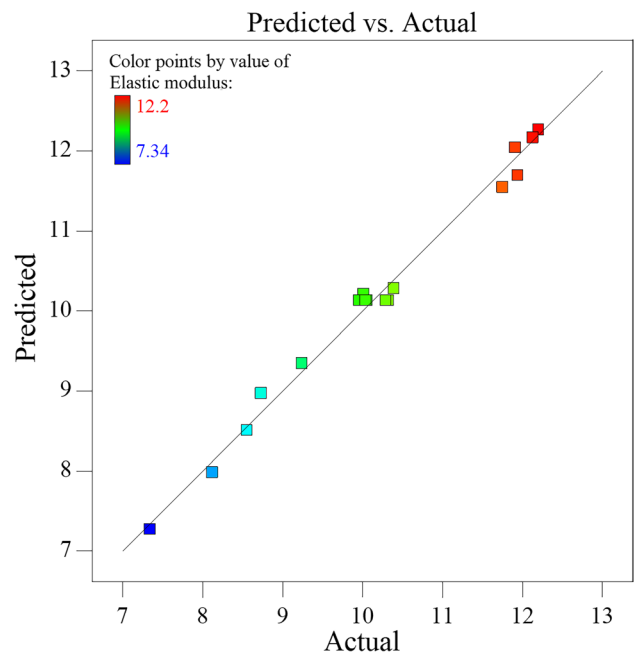
m is the measured sample quality, ρ is density of Ti6Al4V(4.43 g/cm³), r is the radius of the sample, and H is the height of the sample. The microstructure of the transition area was observed by scanning electron microscope. As shown in Fig. 7, the fused area of the sample is well connected and without fracture.

According to ISO13314:2011, the DNS300 electronic universal testing machine is used to test the mechanical properties of the sample, the compression feed rate is 3 mm/min, and the sampling frequency is 5 Hz. The experimental data are automatically recorded by the computer, and the force–displacement curve is obtained, which is then converted into a compressive stress–strain curve. From the compressive stress–strain curve, the elastic modulus and yield strength of the sample can be obtained. The elastic modulus of the sample is determined by the slope of the straight line in the linear deformation zone at the beginning of the curve, and the yield
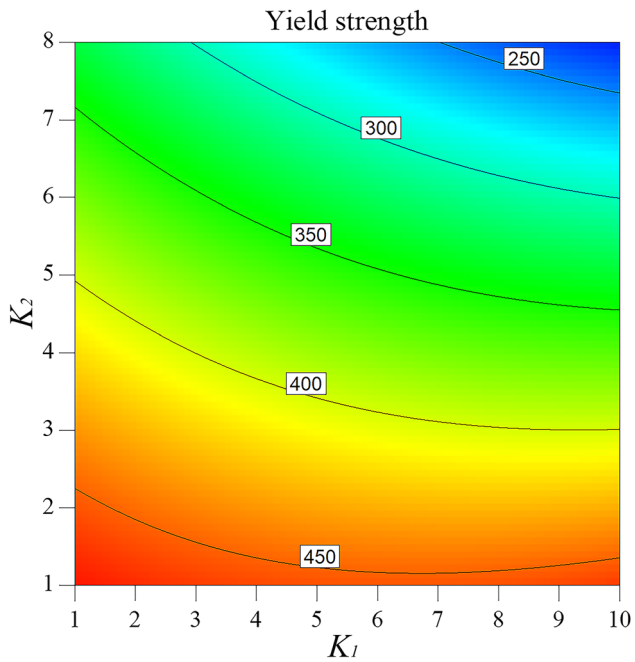
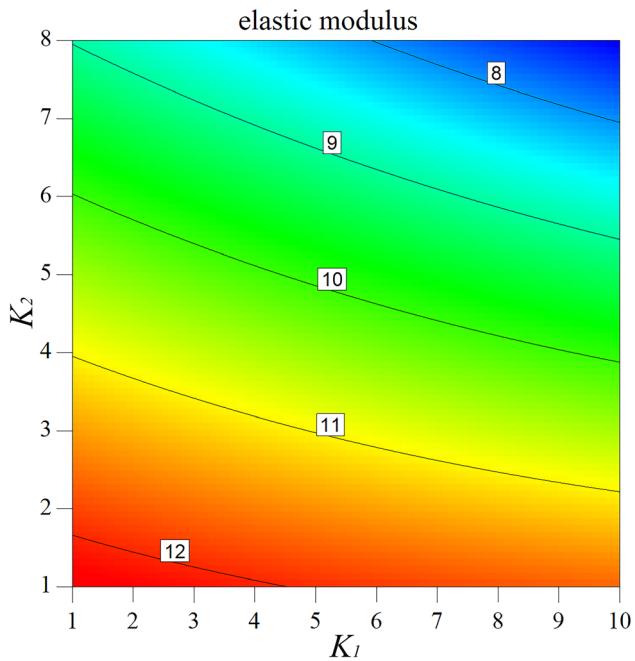**Fig. 10** Response surface contour of yield strength

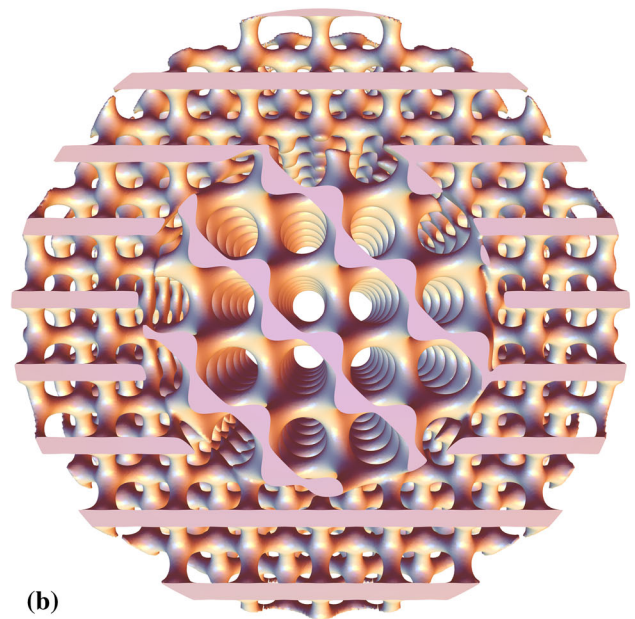**Fig. 11** Response surface contour of elastic modulus

(a)

(b)

Fig. 12 (a) $K_1 = 1$, $K_2 = 1$, $r = 5.25$. (b) $K_1 = 10$, $K_2 = 8$, $r = 5.25$

strength is measured on the compressive stress–strain curve using the 0.2% offset method.

2.5 Experimental Design

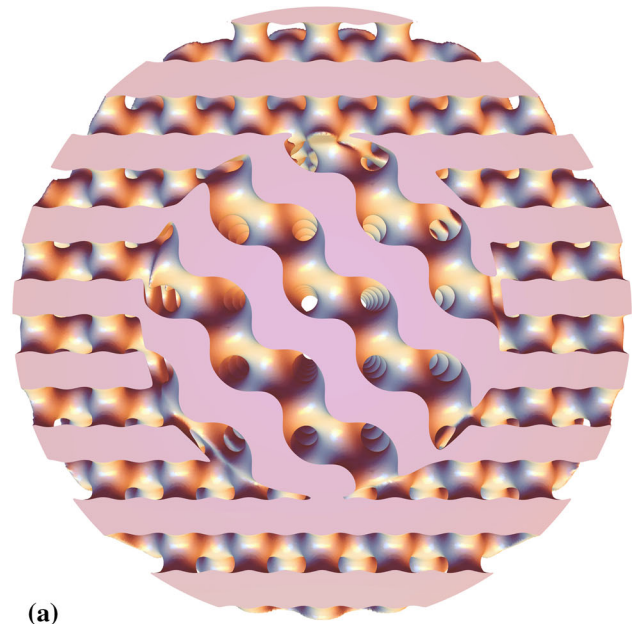The response surface method can effectively optimize the design parameters by studying the interaction between the structure design parameters and the response values, carrying out analysis of variance, and determining the regression coefficients to prove the influence of the design parameters on the response value (Ref 28). The goal of the research is to maximize the yield strength while minimizing the elastic modulus when the porosity meets a certain range.

The Box–Behnken method of Design-Expert software (Version 10.0) is used to study the effects of G unit constant (K_1), D unit constant (K_2), and fused boundary (r) on yield strength, elastic modulus, and porosity of the formed part. The levels of each factor are -1, 0, 1, and the factor levels are shown in Table 2.

Fig. 14 The predicted value and actual value of porosity
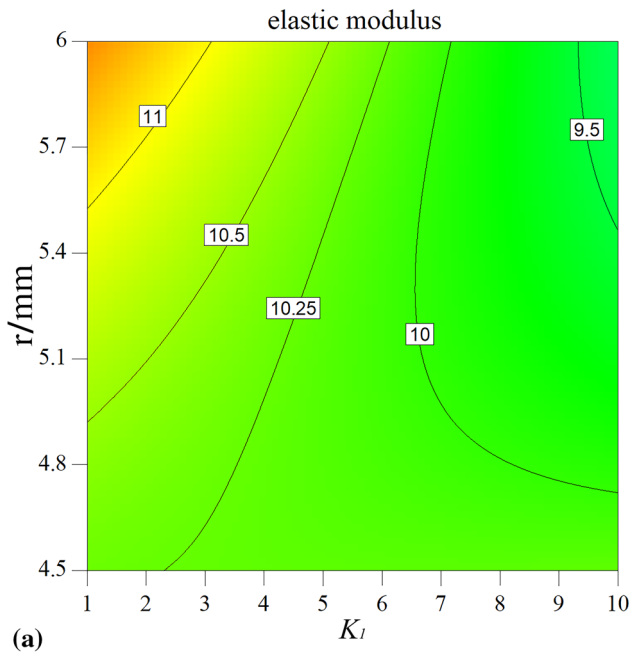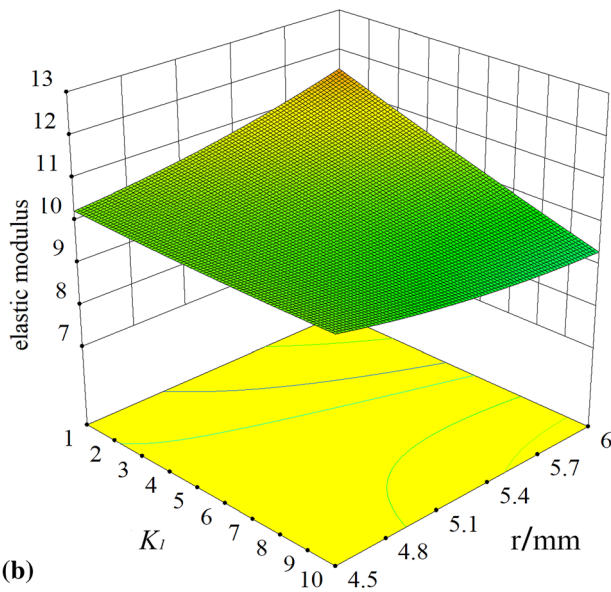
Fig. 13 (a) Response surface contour of elastic modulus. (b) The influence of K_l and r on elastic modulus

3. Results and Analysis

3.1 Experimental Results and Analysis of Variance

After SLM successfully fabricated the samples and conducted the compression test, the relevant measured data are shown in Table 3. The yield strength of the samples is in the range of 219.16–475.72 MPa, the corresponding elastic modulus is in the range of 7.34–12.2 GPa, and the porosity is in the range of 49.82–76.63%.

The Design-Expert software version 10.0 was used to perform regression analysis on the response surface method (RSM) experimental results in Table 3, establishing a response model of poro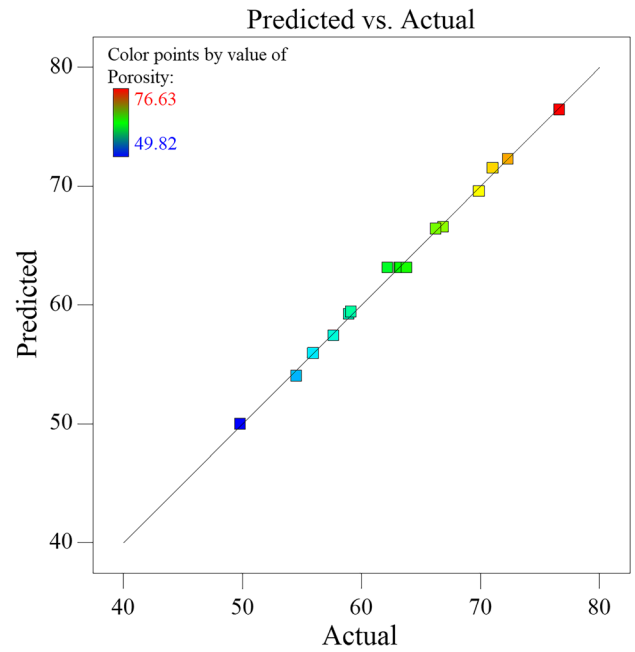us structure parameters and yield strength, elastic modulus, porosity based on the test results, and conducting a significant test of the model.

The variance analysis of yield strength, elastic modulus and porosity is shown in Tables 4, 5, and 6. From Table 4, it can be seen that the adjusted R-squared is 0.9687, the predicted R-squared is 0.8388, and the difference between the them is 0.1299 (less than 0.2), the p value of the lack-of-fit term is 0.1444 (p value is greater than 0.05), and the signal-to-noise ratio is 24.667, which shows that the established model can better express the influence relationship of design parameters on the porous structure. The significant level F value of yield strength model is 56.02, $P > F$ value is less than 0.0001, indicating that the fitting formula of regression model has good fitting accuracy. Similarly, by analyzing Tables 5 and 6, the models of elastic modulus and porosity can also better reflect the influence of design parameters on porous structure. The fitted models of yield strength, elastic modulus, and porosity are shown in Eq. 8, 9 and 10.

The fitted models of yield strength are:

$$y_1 = 109.65749 + 34.79181 \times K_1 - 50.45177 \times K_2$$
$$+ 133.67148 \times r - 1.50444 \times K_1 \times K_2 - 7.66667$$
$$\times K_1 \times r + 7.33619 \times K_2 \times r + 0.53559 \times K_1^2$$
$$- 0.73443 \times K_2^2 - 11.70089 \times r^2$$

$$(\text{Eq 8})$$

The fitted models of elastic modulus are:

$$y_2 = 17.2734 + 0.75836 \times K_1 - 0.68612 \times K_2 - 2.45546$$
$$\times r - 0.017937 \times K_1 \times K_2 - 0.15778 \times K_1 \times r$$
$$+ 0.061905 \times K_2 \times r + 2.23457 \times 10^{-3} \times K_1^2$$
$$- 0.010184 \times K_2^2 + 0.30267 \times r^2$$

$$(\text{Eq 9})$$
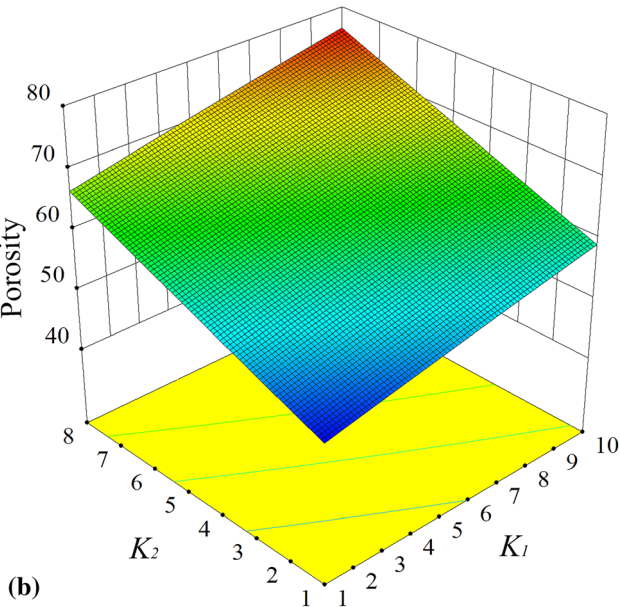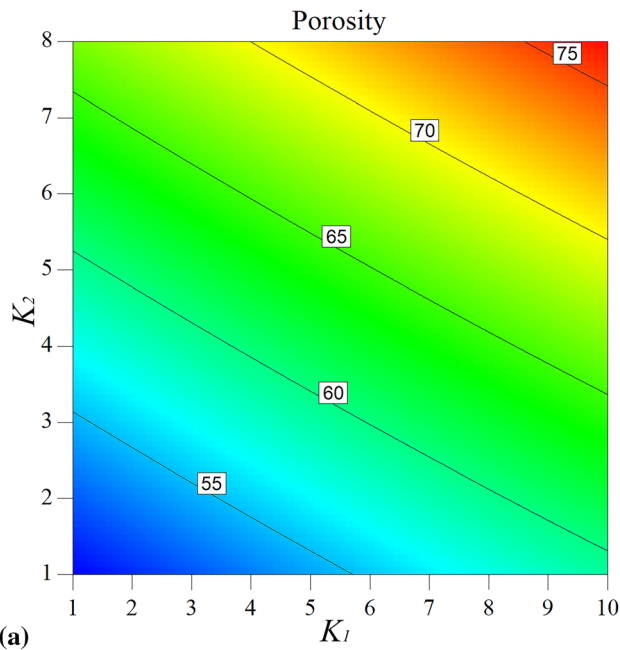
The fitted models of porosity are:

Fig. 15 (a) Response surface contour of porosity. (b) K_1 and K_2 influence on porosity

$$
\begin{aligned}
y_3 = {} & 60.56941 - 0.88332 \times K_1 + 3.64891 \times K_2 - 4.78695 \\
& \times r + 9.84127 \times 10^{-3} \times K_1 \times K_2 + 0.37852 \times K_1 \times r \\
& - 0.25524 \times K_2 \times r - 7.79012 \times 10^{-3} \times K_1^2 + 5.69388 \\
& \times 10^{-3} \times K_2^2 + 0.404 \times r^2
\end{aligned}
$$

$$\text{(Eq 10)}$$

3.2 Analysis of Mechanical Properties

It can be seen from Fig. 8 and 9 that all the data points are distributed near the reference line, and the predicted value is very close to the actual value. The predicted value of the model is basically distributed on the actual value line. The determi-

nation coefficient R^2 of the yield strength model is 0.9863, and the determination coefficient R^2 of the elastic modulus model is 0.9891. In summary, it is shown that the mechanical model fits well and can provide an effective basis for predicting and controlling the mechanical properties of the sample.

Figure 10 and 11 shows the effect of the interaction of K_1 and K_2 on the yield strength and elastic modulus in the form of contour lines and their three-dimensional response surfaces. It can be seen that with the simultaneous increase of K_1 and K_2, the yield strength and elastic modulus are gradually reduced, because with the increase of K_1 and K_2, the rod diameters of the G and D units decrease, and the relative density of the sample changed under the limitation of the size of the unit bounding box. According to the Gibson–Ashby theoretical model, it is found that there is a power function relationship between the mechanical properties of porous materials and the relative density, and both will increase with the increase of relative density (Ref 29). As shown in formulas (11) and (12), where E_c, σ_c, and ρ^* are the elastic modulus (GPa), yield strength (MPa) and density (g/mm^3) of the porous structure, E_s, σ_s, and ρ_s are the elastic modulus (GPa), yield strength (MPa), and density (g/mm^3) of the dense body material, ρ^*/ρ_s is the relative density, C_1, C_2 and m_1, m_2 are geometric proportional constants. As shown in Fig. 12, when the same fused boundary $r = 5.25$ and different K values ($K_1 = 1$, $K_2 = 1$ and $K_1 = 10$, $K_2 = 8$). It can be seen that when the K value changes, the relative density of the two TPMS units changes, which affects the mechanical properties of the overall structure.

$$\frac{E^*}{E_s} = C_1 \left(\frac{\rho^*}{\rho_s} \right)^{m_1} \tag{Eq 11}$$

$$\frac{\sigma^*}{\sigma_s} = C_2 \left(\frac{\rho^*}{\rho_s} \right)^{m_2} \tag{Eq 12}$$

Figure 13 shows the influence of the interaction of K_1 and r on the elastic modulus in the form of contour lines and its three-dimensional response surface. When the fused boundary remains unchanged, with the increase of K_1, the elastic modulus gradually decreases, which conforms to the law of Gibson–Ashby theoretical model. At a relatively small K_1, the elastic modulus gradually increases with the increase of r, while at a larger K_1, the elastic modulus changes slowly, because the G unit has a different rate of change of elastic modulus under different K values. The change rate of elastic modulus is greater at a smaller value of K, and the change rate of elastic modulus is smaller at a larger value of K (Ref 14).

Metal bone scaffolds need to have sufficient strength to transfer mechanical loads without producing large deformations that may endanger the fixation of the bone scaffolds (Ref 30). It can be seen from Table 3 that the yield strength of the sample is in the range of 219.16–475.72 MPa, and the corresponding modulus of elasticity is in the range of 7.34–12.2 GPa, which is greater than the compressive strength of human tibia and is equivalent to the modulus of elasticity (Ref 31). Therefore, the use of the fused TPMS porous structure can not only meet the needs of bearing external loads, but also effectively reduce the stress shielding effect.

3.3 Analysis of Porosity

All the data points in Fig. 14 are distributed near the reference line, the predicted value is very close to the actual

value. The predicted value of the model is basically distributed on the actual value line, and the coefficient of determination R^2 is 0.9969. In conclusion, the porosity model fits well and can provide an effective basis for the prediction and control of the porosity of the sample.

Figure 15 shows the effect of K_1 and K_2 interaction on porosity in the form of contour lines and its three-dimensional response surface. It can be seen that as K_1 and K_2 increase at the same time, the porosity gradually increases, because K_1 and K_2 are the constant values in the G and D expressions, respectively. Changing the constant value will affect the shape of the TPMS isosurface and then affect generated G and D units, as shown in Fig. 16. The fused boundary r has little effect on the porosity of the sample, because when K_1 and K_2 are determined, the fused boundary r will affect the pores at the fused area and the volume occupied by the G unit. However, the pores of the fused part and the occupied volume change very little, so the overall porosity of the sample has little influence. In addition, there is unmelted titanium alloy powder on the surface of the sample printed by SLM, which will also affect the porosity. The reason for this situation is that when the unmelted powder approaches the melting area, the temperature difference between the two is
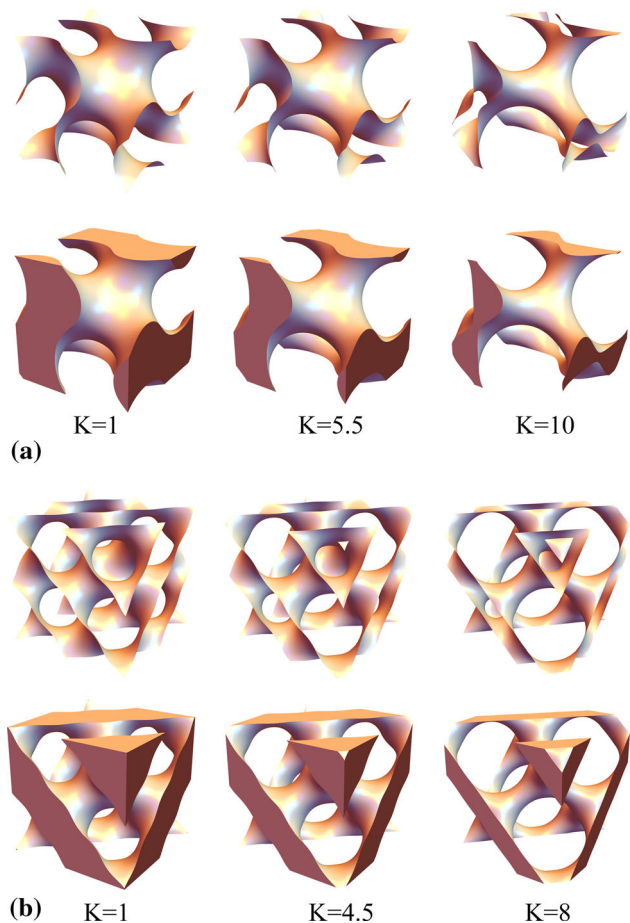

Fig. 16 (a) Gyroid isosurface and unit structure with different K values. (b) Diamond isosurface and unit structure with different K values
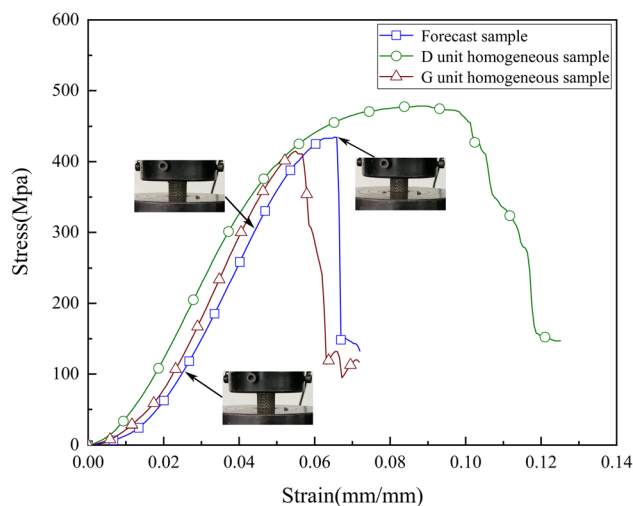

Fig. 17 Stress–strain diagrams of the compression experiments

Table 7 Optimization standards and targets

Variable/response	Input/output	Standard	Level		Importance
			Low level	High level	
Variable	K_1	Maximize	1	10	3
	K_2	Minimize	1	8	3
	r(mm)	range	4.5	6	3
Response	Yield strength	Maximize	219.16	475.72	3
	Elastic modulus	Minimize	7.34	12.2	3
	Porosity	Range	49.82	76.63	3

Table 8 Prediction and verification

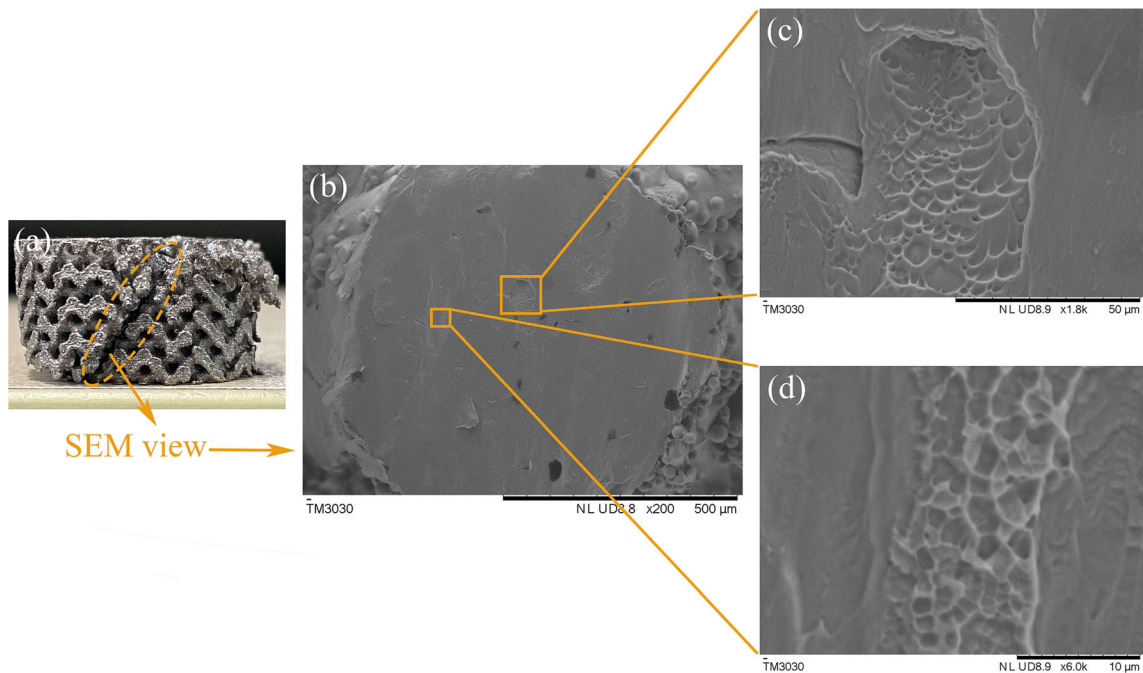|	K_1	K_2	r	Yield strength	Apparent elastic modulus	Porosity	Desirability
Predict	10.000	2.656	5.564	395.372	10.554	64.111	0.649
Experimental	10.000	2.656	5.564	400.962	10.532	64.027	

Fig. 18 SEM micrographs of fractured surface on the failed sample

very large. Due to the effect of thermal diffusion, the powder will inevitably adhere to the surface of sample (Ref 32), which is also confirmed by Wally et al. (Ref 33). Some clinical and in vitro studies have shown that the surface morphology of implants can also affect the biological response of bone. The unmelted powder affects the surface roughness of the implant, which may help to enhance cell diffusion and promote bone tissue integration (Ref 34). It can be seen from Table 3 that the porosity of almost all samples is above 50%. Higher porosity can improve the transport capacity of oxygen and nutrients, promote bone integration and repair bone injury (Ref 35, 36).

3.4 Optimization of Design Parameters and Test Verification

In order to obtain the ideal fused porous structure, the response models of yield strength, elastic modulus, and porosity established in the previous section need to be optimized by multi-objectives. The design parameters K_1 are maximize and K_2 are minimize. The purpose is to make the fused porous structure more in line with the pore distribution of bone tissue. The goal of optimization is to maximize the yield strength while minimizing the elastic modulus. The porosity is within the design range. The optimization criteria and goals are shown in Table 7. All design parameters and response value levels are designated as default values 3. After optimization, $K_1 = 10.000$, $K_2 = 2.656$, and $r = 5.564$ are selected as the most ideal design parameters. The predicted values and experimental verification values of yield strength, elastic modulus and porosity are shown in Table 8.

According to the optimized structure, the porous structure was fabricated, and the optimized results were verified by experiments. The measured yield strength of the optimized structure is 400.962 Mpa, the elastic modulus is 10.532 GPa, and the porosity is 64.027%. For the yield strength, the errors of

elastic modulus, and porosity are 1.414%, 0.208%, and 0.131%, respectively. There is little difference between the optimized result and the predicted result. Therefore, the proposed mathematical models of yield strength, elastic modulus, and porosity can provide theoretical guidance for the control and prediction of the mechanical properties of the fused porous structure.

The stress–strain curve of the predicted sample is shown in Fig. 17. It can be seen that there is a nonlinear area at the beginning of the stress–strain curve, which is caused by the fact that the end face of the sample is not completely parallel to the placement platform (Ref 37). In addition, the stress of the sample increases first increases sharply, then slowly increases, then increases slowly until the compressive strength is reached, and then drops sharply after exceeding the compressive strength. Figure 17 shows that the predicted samples are found to have higher yield strength and lower elastic modulus compared with the homogeneous porous samples of G and D units with 65% porosity. It shows that compared with homogeneous porous structure, porous structure with better bone tissue structure and excellent mechanical properties can be designed by fusing two TPMS units.

As shown in Fig. 18, the failed sample after the compression test was observed. The sample has shear fracture (Fig. 18a). Similar results have been observed in other references (Ref 38, 39), and the failed mode is related to the geometry of the unit (Ref 40). The fracture surface is observed by scanning electron microscope. The fracture surface shows smooth fracture characteristics and multiple shallow dimples (Fig. 18c and d), showing a mixed failed mode, which may have an adverse impact on the mechanical properties of the structure, but the ductile shear fracture of the sample can effectively ensure the continuous absorption of energy.

4. Conclusion

In this research, we designed a porous structure suitable for bone tissue structure by fusing two types of TPMS units, and the effects of design parameters on yield strength, elastic modulus, and porosity were analyzed by the response surface method, which provided a theoretical basis for the prediction and control of mechanical properties of fused porous structure. This research drew the following conclusions:

1. The fused porous structures manufactured by SLM show good mechanical properties. The outer region of the fused porous structure has high bearing capacity, and the inner region provides a place for cell growth, which well simulates the structure of natural bone tissue. The yield strength of the samples is 219.16–475.72 Mpa, which is greater than compressive strength of human tibia, and the elastic modulus is 7.34–12.2 GPa, which is equivalent to elastic modulus of human tibia. It can satisfy the mechanical properties requirements of human bones. The porosity is 49.82–76.63%, which is conducive to the proliferation and differentiation of bone cells.

2. The constant K_1 of Gyroid unit and the constant K_2 of Diamond unit are the main factors affecting the mechanical properties and porosity of porous structure. The yield strength and elastic modulus decrease with the increase of constants K_1 and K_2, while the porosity increases with the increase of constants K_1 and K_2. The fused boundary r has a small influence on the mechanical properties and porosity.

3. The optimized structural parameters are as follows: constant $K_1 = 10.000$, constant $K_2 = 2.656$, and fused boundary $r = 5.564$ mm. The fused TPMS porous structure was fabricated with the optimal structural parameters. Its yield strength is 400.962 MPa, elastic modulus is 10.532 GPa, and porosity is 64.027%, which shows little difference from the predicted results. Therefore, Ti6Al4V porous structure with high strength and low elastic modulus can be fabricated by fusing TPMS and selective laser melting technology.

Author Contributions

SZ: Conceptualization, Writing—review & editing, Supervision, Funding acquisition. WH: Methodology, Validation, Formal analysis, Investigation, Writing—original draft. JW: Investigation, Visualization. MX: Conceptualization, Supervision. TW: Conceptualization, Supervision.

Funding

Conflict of interest

The authors declare no conflict of interest.

References

1. J.J. Li, M. Ebied, J. Xu and H. Zreiqat, Current Approaches to Bone Tissue Engineering: The Interface Between Biology and Engineering, *Adv. Healthc. Mater.*, 2018, **7**, 1701061.
2. H.D. Jung, Titanium and Its Alloys for Biomedical Applications, *Metals.*, 2021, **11**, p 1945–1945.
3. F. Bartolomeu, N. Dourado, F. Pereira, N. Alves, G. Miranda and F.S. Silva, Additive Manufactured Porous Biomaterials Targeting Orthopedic Implants: A Suitable Combination of Mechanical, Physical and Topological Properties, *Mater. Sci. Eng. C.*, 2020, **107**, 110342.
4. H.X. Liang, Y.W. Yang, D.Q. Xie, L. Li, N. Mao, C.J. Wang, Z.J. Tian, Q. Jiang and L.D. Shen, Trabecular-Like Ti-6Al-4V Scaffolds for Orthopedic: Fabrication by Selective Laser Melting and In Vitro Biocompatibility, *J. Mater. Sci. Technol.*, 2019, **35**, p 1284–1297.
5. D. Melancon, Z.S. Bagheri, R.B. Johnston, L. Liu, M. Tanzer and D. Pasini, Mechanical Characterization of Structurally Porous Biomaterials Built Via Additive Manufacturing: Experiments, Predictive Models, and Design Maps for Load-Bearing Bone Replacement Implants, *Acta Biomater.*, 2017, **63**, p 350–368.
6. H. Lee, M.K. Lee, G. Han, H.E. Kim, J.H. Song, Y. Na, C.B. Yoon, S.K. Oh, T.S. Jang and H.D. Jung, Customizable Design of Multiple-Biomolecule Delivery Platform for Enhanced Osteogenic Responses Via 'Tailored Assembly System,' *Bio-Des. Manuf.*, 2022, **5**, p 451–464.
7. H. Lee, M.K. Lee, K.H. Cheon, I.G. Kang, C.I. Park, T.S. Jang, G. Han, H.E. Kim, J.H. Song and H.D. Jung, Functionally Assembled Metal Platform as Lego-Like Module System for Enhanced Mechanical Tunability and Biomolecules Delivery, *Mater. Des.*, 2021, **207**, 109840.
8. K.K. Sahu and Y.K. Modi, Investigation on Dimensional Accuracy, Compressive Strength and Measured Porosity of Additively Manufactured Calcium Sulphate Porous Bone Scaffolds, *Mater. Technol.*, 2021, **36**, p 492–503.
9. F.Y. Deng, L.L. Liu, Z. Li and J.C. Liu, 3D Printed Ti6Al4V Bone Scaffolds with Different Pore Structure Effects on Bone Ingrowth, *J. Biol. Eng.*, 2021, **15**, p 1–13.
10. H. Lee, H.D. Jung, M.H. Kang, J.H. Song, H.E. Kim and T.S. Jang, Effect of HF/HNO3-Treatment on the Porous Structure and Cell Penetrability of Titanium (Ti) Scaffold, *Mater. Des.*, 2018, **145**, p 65–73.
11. C. Wang, D.L. Xu, L. Lin, S.J. Li, W.T. Hou, Y. He, L.Y. Sheng, C. Yi, X.L. Zhang, H.Y. Li, Y.M. Li, W. Zhao and D.S. Yu, Large-Pore-Size Ti6Al4V Scaffolds with Different Pore Structures for Vascularized Bone Regeneration, *Mater. Sci. Eng. C.*, 2021, **131**, p 112499–112499.
12. M.A. El-Sayed, K. Essa, M. Ghazy and H. Hassanin, Design Optimization of Additively Manufactured Titanium Lattice Structures for Biomedical Implants, *Int. J. Adv. Manuf. Technol.*, 2020, **110**, p 1–12.
13. S.R.D. Galarreta, R.J. Doyle, J. Jeffers and S. Ghouse, Laser powder Bed Fusion of Porous Graded Structures: A Comparison Between Computational and Experimental Analysis, *J. Mech. Behav. Biomed. Mater.*, 2021, **123**, p 104784–104784.
14. X.Y. Zheng, Z.B. Fu, K. Du, C.Y. Wang and Y. Yi, Minimal Surface Designs for Porous Materials: From Microstructures to Mechanical Properties, *J. Mater. Sci.*, 2018, **53**, p 10194–10208.
15. D.W. Li, W.H. Liao, N. Dai and Y.M. Xie, Comparison of Mechanical Properties and Energy Absorption of Sheet-Based and Strut-Based Gyroid Cellular Structures with Graded Densities, *Materials.*, 2019, **12**, p 2183–2183.
16. L. Yang, C.Z. Yan, C.J. Han, P. Chen, S.F. Yang and Y.S. Shi, Mechanical Response of a Triply Periodic Minimal Surface Cellular Structures Manufactured by Selective Laser Melting, *Int. J. Mech. Sci.*, 2018, **148**, p 149–157.
17. F.S.L. Bobbert, K. Lietaert, A.A. Eftekhari, B. Pouran, S.M. Ahmadi, H. Weinans and A.A. Zadpoor, Additively Manufactured Metallic

Porous Biomaterials Based on Minimal Surfaces: A Unique Combination of Topological, Mechanical, and Mass Transport Properties, *Acta Biomater.*, 2017, **53**, p 572–584.

18. L. Yang, R. Mertens, M. Ferrucci, C.Z. Yan, Y.S. Shi and S.F. Yang, Continuous Graded Gyroid Cellular Structures Fabricated by Selective Laser Melting: Design, Manufacturing and Mechanical Properties, *Mater. Des.*, 2019, **162**, p 394–404.

19. M.A. Surmeneva, R.A. Surmenev, E.A. Chudinova, A. Koptioug, M.S. Tkachev, S.N. Gorodzha and L.E. Rännar, Fabrication of Multiple-Layered Gradient Cellular Metal Scaffold Via Electron Beam Melting for Segmental Bone Reconstruction, *Mater. Des.*, 2017, **133**, p 195–204.

20. Y.Z. Xiong, R.N. Gao, H. Zhang, L.L. Dong, J.T. Li and X. Li, Rationally Designed Functionally Graded Porous Ti6Al4V Scaffolds with High Strength and Toughness Built Via Selective Laser Melting for Load-Bearing Orthopedic Applications, *J. Mech. Behav. Biomed. Mater.*, 2020, **104**, 103673.

21. T.S. Jang, D.E. Kim, G. Han, C.B. Yoon and H.D. Jung, Powder Based Additive Manufacturing for Biomedical Application of Titanium and Its Alloys: A Review, *Biomed. Eng. Lett.*, 2020, **10**, p 505–516.

22. S. Dhiman, S.S. Sidhu and P.S. Bains, Mechanobiological Assessment of Ti-6Al-4V Fabricated Via Selective Laser Melting Technique: A Review, *Rapid. Prototyping. J.*, 2019, **25**, p 1266–1284.

23. C.Y. Yap, C.K. Chua, Z.L. Dong, Z.H. Liu, D.Q. Zhang, L.E. Loh and S.L. Sing, Review of Selective Laser Melting: Materials and Applications, *Appl. Phys. Rev.*, 2015, **2**, 041101.

24. M.K. Zhang, Y.Q. Yang, W.T. Qin, S.B. Wu, J. Chen and C.H. Song, Optimizing the Pinch-Off Problem for Gradient Triply Periodic Minimal Surface Cellular Structures Manufactured by Selective Laser Melting, *Rapid. Prototyping. J.*, 2020, **26**, p 1771–1781.

25. E. Yang, M. Leary, B. Lozanovski, D. Downing, M. Mazur, A. Sarker, A.M. Khorasani, A. Jones, T. Maconachie, S. Bateman, M. Easton, M. Qian, P. Choong and M. Brandt, Effect of Geometry on the Mechanical Properties of Ti-6Al-4V Gyroid Structures Fabricated Via SLM: A Numerical Study, *Mater. Des.*, 2019, **184**, p 108165–108165.

26. S.J. Hollister and N. Kikuchi, Homogenization Theory and Digital Imaging: A Basis for Studying the Mechanics and Design Principles of Bone Tissue, *Biotechnol. Bioeng.*, 1994, **43**, p 586–596.

27. N. Yang, Z. Quan, D.W. Zhang and Y.L. Tian, Multi-Morphology Transition Hybridization CAD Design of Minimal Surface Porous Structures for Use in Tissue Engineering, *Comput. Aided. Design.*, 2014, **56**, p 11–21.

28. B.B. Ravichander, A. Amerinatanzi and N.S. Moghaddam, Study on the Effect of Powder-Bed Fusion Process Parameters on the Quality of as-Built IN718 Parts Using Response Surface Methodology, *Metals.*, 2020, **10**, p 1180–1180.

29. M. Dumas, P. Terriault and V. Brailovski, Modelling and Characterization of a Porosity Graded Lattice Structure for Additively Manufactured Biomaterials, *Mater. Des.*, 2017, **121**, p 383–392.

30. S. Amin Yavari, R. Wauthle, J. van der Stok, A.C. Riemslag, M. Janssen, M. Mulier, J.P. Kruth, J. Schrooten, H. Weinans and A.A. Zadpoor, Fatigue Behavior of Porous Biomaterials Manufactured Using Selective Laser Melting, *Mater. Sci. Eng. C*, 2013, **33**, p 4849–4858.

31. X.Z. Zhang, M. Leary, H.P. Tang, T. Song and M. Qian, Selective Electron Beam Manufactured Ti-6Al-4V Lattice Structures for Orthopedic Implant Applications: Current Status and Outstanding Challenges, *Curr. Opin. Solid State Mater. Sci.*, 2018, **22**, p 75–99.

32. D.L. Zhao, Y.T. Huang, Y. Ao, C.J. Han, Q. Wang, Y. Li, J. Liu, Q.S. Wei and Z. Zhang, Effect of Pore Geometry on the Fatigue Properties and Cell Affinity of Porous Titanium Scaffolds Fabricated by Selective Laser Melting, *J. Mech. Behav. Biomed. Mater.*, 2018, **88**, p 478–487.

33. Z.J. Wally, A.M. Haque, A. Feteira, F. Claeyssens, R. Goodall and G.C. Reilly, Selective Laser Melting Processed Ti6Al4V Lattices with Graded Porosities for Dental Applications, *J. Mech. Behav. Biomed. Mater.*, 2018, **90**, p 20–29.

34. M.D. Wild, R. Schumacher, K. Mayer, E. Schkommodau, D. Thoma, M. Bredell, A.K. Gujer, K.W. Grätz and F.E. Weber, Bone Regeneration by the Osteoconductivity of Porous Titanium Implants Manufactured by Selective Laser Melting: A Histological and Micro Computed Tomography Study in the Rabbit, *Tissue Eng. Part. A.*, 2013, **19**, p 2645–2654.

35. N. Taniguchi, S. Fujibayashi, M. Takemoto, K. Sasaki, B. Otsuki, T. Nakamura, T. Matsushita, T. Kokubo and S. Matsuda, Effect of Pore Size on Bone Ingrowth into Porous Titanium Implants Fabricated by Additive Manufacturing: An In Vivo Experiment, *Mater. Sci. Eng. C.*, 2016, **59**, p 690–701.

36. L. Li, J.P. Shi, K.J. Zhang, L.F. Yang, F. Yu, L.Y. Zhu, H.X. Liang, X.S. Wang and Q. Jiang, Early Osteointegration Evaluation of Porous Ti6Al4V Scaffolds Designed Based on Triply Periodic Minimal Surface Models, *J. Orthop. Translat.*, 2019, **19**, p 94–105.

37. S. Ma, Q. Tang, Q.X. Feng, J. Song, X.X. Han and F.Y. Guo, Mechanical Behaviours and Mass Transport Properties of Bone-Mimicking Scaffolds Consisted of Gyroid Structures Manufactured Using Selective Laser Melting, *J. Mech. Behav. Biomed. Mater.*, 2019, **93**, p 158–169.

38. D.L. Zhao, H. Liang, C.J. Han, J.J. Li, J. Liu, K. Zhou, C. Yang and Q.S. Wei, 3D Printing of a Titanium-Tantalum Gyroid Scaffold with Superb Elastic Admissible Strain, Bioactivity and In-Situ Bone Regeneration Capability, *Addit. Manuf.*, 2021, **47**, 102223.

39. G.S. Yu, Z.B. Li, S.J. Li, Q. Zhang, Y.L. Hua, H. Liu, X.Y. Zhao, D.T. Dhaidhai, W. Li and X.J. Wang, The Select of Internal Architecture for Porous Ti Alloy Scaffold: A Compromise Between Mechanical Properties and Permeability, *Mater. Des.*, 2020, **192**, 108754.

40. X.J. Fan, Q. Tang, Q.X. Feng, S. Ma, J. Song, M.X. Jin, F.Y. Guo and P. Jin, Design, Mechanical Properties and Energy Absorption Capability of Graded-Thickness Triply Periodic Minimal Surface Structures Fabricated by Selective Laser Melting, *Int. J. Mech. Sci.*, 2021, **204**, 106586.

Publisher's Note Springer Nature remains neutral with regard to jurisdictional claims in published maps and institutional affiliations.